IOPscience iopscience.iop.org

Home Search Collections Journals About Contact us My IOPscience

Design of piezoresistive versus piezoelectric contact mode scanning probes

This article has been downloaded from IOPscience. Please scroll down to see the full text article.

2010 J. Micromech. Microeng. 20 095023

(http://iopscience.iop.org/0960-1317/20/9/095023)

View the table of contents for this issue, or go to the journal homepage for more

Download details:
IP Address: 171.67.216.21
The article was downloaded on 18/08/2010 at 04:18

Please note that terms and conditions apply.

J. Micromech. Microeng. **20** (2010) 095023 (15pp) doi:10.1088/0960-1317/20/9/095023

Design of piezoresistive versus piezoelectric contact mode scanning probes

Joseph C Doll and Beth L Pruitt

Department of Mechanical Engineering, Stanford University, Stanford, CA, USA

E-mail: pruitt@stanford.edu

Received 6 June 2010, in final form 12 July 2010
Published 17 August 2010
Online at stacks.iop.org/JMM/20/095023

Abstract

Microfabricated cantilever scanning probes are used for a variety of technological applications. Piezoresistivity and piezoelectricity are two transduction mechanisms that are commonly used to sense cantilever deflection. Despite their widespread use, their performance has not been directly compared to date. In this paper we present detailed models for the noise and sensitivity of both transducer types, design optimized cantilevers via numerical optimization for a variety of use cases, and compare their performance using a range of reported values in the literature. We find that piezoresistive sensing is advantageous for sub-micron thick cantilevers and moderate electrical power dissipation conditions, while piezoelectric sensing is preferred for thick cantilevers and power-limited applications. The wide variability in experimentally measured piezoelectric film properties is treated using the Monte Carlo method and can account for resolution variation of up to 30%, independent of geometric tolerances. We find that the preferred cantilever type depends heavily upon the fabrication and operating constraints. Accordingly, the modeling and optimization code is an open source and freely available. Importantly, we show that both piezoresistive and piezoelectric cantilevers are capable of sensing piconewton and sub-nanometer signals for a wide range of operating conditions with an appropriate design.

(Some figures in this article are in colour only in the electronic version)

1. Introduction

The atomic force microscope (AFM) is widely used to characterize surface structures and forces. Since the first system using optically detected cantilever beam deflection [1], a variety of microelectromechanical systems (MEMS) scanning probes have been developed to modify the functionality of the AFM. Alternative sensing techniques include capacitive [2, 3], thermal [4, 5], piezoresistive [6, 7] and piezoelectric [8, 9] transduction.

Piezoresistive and piezoelectric transduction have many similarities: they do not require optics, work for a wide variety of samples and measurement conditions, and their fabrication processes are well suited for forming cantilever structures for out-of-plane operation. Recent review articles on piezoresistive [10] and piezoelectric [11] MEMS sensors introduce the fundamental concepts but are not specific enough to discuss the design of scanning probes. Their performance has been indirectly compared in a literature survey [12], but differences in fabrication methods, measurement techniques and design goals complicate such comparisons. In this paper we provide a fundamental design comparison of piezoresistive and piezoelectric microcantilever beams optimized for force or displacement sensing.

The transduction principle for both sensor types is that a force applied at the tip of the cantilever beam induces a deflection, curvature and bending stress in the cantilever. The stress can be transformed into a measurable signal by either the piezoresistive or piezoelectric effect. A piezoresistor typically transduces the longitudinal stress as a change in resistivity proportional to its longitudinal piezoresistive coefficient, π_l, while a piezoelectric typically transduces the longitudinal stress as a polarization charge proportional to its transverse piezoelectric coefficient, d_{31}.

The design optimization of piezoresistive cantilevers has been studied extensively [13–16]. Similarly, the analysis and

 © 2010 IOP Publishing Ltd Printed in the UK & the USA

optimal design of piezoelectric actuators [17, 18] has been extensively reported, in addition to more general overviews [19, 20]. While the typical displacement resolution of microscale sensors has been compared [21], the design optimization of piezoelectric sensors has focused on sensitivity maximization [18, 22, 23] and the detection of force gradients [24] rather than the minimum detectable force (MDF) or displacement (MDD). The design optimization we present consists of choosing the best possible design parameters for a fixed set of constraints to minimize the MDF or MDD.

Piezoelectric transduction has several unique characteristics that are ideal for scanning probes, including efficient actuation [25] and simultaneous actuation and sensing [26, 27]. Advantages of on-chip actuation include the ability to scale to large cantilever arrays [28] and apply forces or perform feedback control at high frequency [29]. Although resonant piezoelectric detection leads to superior performance for certain dynamic applications like the tapping mode AFM [30–32], we have focused on broadband sensing (i.e. contact mode) which can be used to investigate samples, such as living cells [33], over a larger range of timescales.

We make several assumptions about the cantilever fabrication processes. For ease of comparison and analysis, we assume that the piezoresistor is grown via epitaxy and boron doped. Epitaxy is an additive process but the same analysis techniques can be applied to diffusion or ion implantation doping, which do not affect the beam thickness, with comparable results [15, 16].

We assume that the piezoelectric transducer is a polycrystalline piezoelectric film deposited on a single crystal silicon cantilever beam and sandwiched between metal electrodes of finite thickness. We consider two popular piezoelectric materials, aluminum nitride (AlN) and lead zirconium titanate (PZT). AlN and PZT have very different material properties and can be deposited using a variety of methods [20]. Representative fabrication processes can be found in [7] and [9].

A signal conditioning circuit is required for both sensor types, and our noise analysis includes intrinsic device noise and amplifier noise as well as thermomechanical noise. The noise and sensitivity are analyzed at the amplifier inputs, and noise from subsequent filtering is not included because it would be common to both sensor types and can be made negligibly small. Second order effects such as metal electrodes and amplifier input capacitance are included in the analysis. Overall, we have aimed to present a realistic assessment of the resolution achievable by each transduction mechanism and to clearly identify situations where one is preferable to the other.

We first develop the sensitivity and noise models for a piezoresistive cantilever, then analyze the piezoelectric cantilever case. Next, we use the models to generate optimized designs using an iterative, computational approach. We have previously demonstrated this approach for the piezoresistive cantilever design [16]. Finally, we use the optimization results and reported material properties to compare sensor performance and discuss the merits of each transduction mechanism.

Table 1. Summary of the variables.

Variable	Description	Units
l_c	Cantilever length	m
w_c	Cantilever width	m
t_c	Cantilever thickness	m
$f_{\min}$	High-pass filter frequency	Hz
$f_{\max}$	Low-pass filter frequency	Hz
f_0	Cantilever resonant frequency	Hz
k	Cantilever spring constant	$\mathrm{N\,m^{-1}}$
m	Cantilever mass	kg
k_b	Boltzmann's constant	$\mathrm{J\,K^{-1}}$
E	Elastic modulus	$\mathrm{N\,m^{-2}}$
σ_l	Longitudinal stress	$\mathrm{N\,m^{-2}}$
Q_M	Mechanical quality factor	–
μ	Carrier mobility	$\mathrm{cm^2\,V\,s^{-1}}$
ρ	Resistivity	Ω cm
ϵ_r	Relative permittivity	–
l_{pr}	Piezoresistor length	m
w_{pr}	Piezoresistor leg width	m
t_{pr}	Piezoresistor thickness	m
n	Doping concentration	$\mathrm{cm^{-3}}$
π_l	Piezoresistance coefficient	$\mathrm{Pa^{-1}}$
V_{bridge}	Bridge bias voltage	V
R_{pr}	Piezoresistor resistance	Ω
W	Dissipated power	W
N	Number of carriers	–
P	Piezoresistance factor	–
γ	Resistance factor	–
β^*	Piezoresistor efficiency factor	–
t_{pe}	Piezoelectric thickness	m
d_{31}	Transverse piezoelectric coefficient	$\mathrm{pC\,N^{-1}}$
C_m	Normalized beam curvature	$\mathrm{m^2\,N^{-1}}$
z_n	Bending neutral axis	m
R_{pe}	Piezoelectric resistance	Ω
C_{pe}	Piezoelectric capacitance	F
V_J	Johnson voltage noise spectral density	$\mathrm{V\,Hz^{-1/2}}$
V_H	Hooge voltage noise spectral density	$\mathrm{V\,Hz^{-1/2}}$
V_{TH}	Thermomech. noise spectral density	$\mathrm{V\,Hz^{-1/2}}$
V_A	Amp. voltage noise spectral density	$\mathrm{V\,Hz^{-1/2}}$
V_{TOT}	Integrated voltage noise	V
Q_J	Johnson charge noise spectral density	$\mathrm{C\,Hz^{-1/2}}$
Q_{TH}	Thermomech. charge spectral density	$\mathrm{C\,Hz^{-1/2}}$
Q_A	Amp. voltage charge spectral density	$\mathrm{C\,Hz^{-1/2}}$
Q_{TOT}	Integrated charge noise	C
F_V/F_Q	Force noise spectral density	$\mathrm{N\,Hz^{-1/2}}$
S_{FV}	Force–voltage sensitivity	$\mathrm{V\,N^{-1}}$
S_{XV}	Displacement–voltage sensitivity	$\mathrm{V\,m^{-1}}$
S_{FQ}	Force–charge sensitivity	$\mathrm{C\,N^{-1}}$
S_{XQ}	Displacement–charge sensitivity	$\mathrm{C\,m^{-1}}$

2. Piezoresistive cantilever analysis

The design and dimensions of the piezoresistive cantilever are illustrated in figure 1(*a*). The overall length, width and thickness of the cantilever are l_c, w_c and t_c, respectively. The *x*-, *y*- and *z*-axes correspond to the longitudinal, transverse and out-of-plane directions of the cantilever, respectively. The variables we use are summarized in table 1.

The piezoresistor extends l_{pr} along the length of the cantilever and is $t_z pr$ in thickness. A narrow gap is included along the length of the piezoresistor to form a resistive loop, and the width of each cantilever leg is $w_{pr} = w_c/2$. The gap

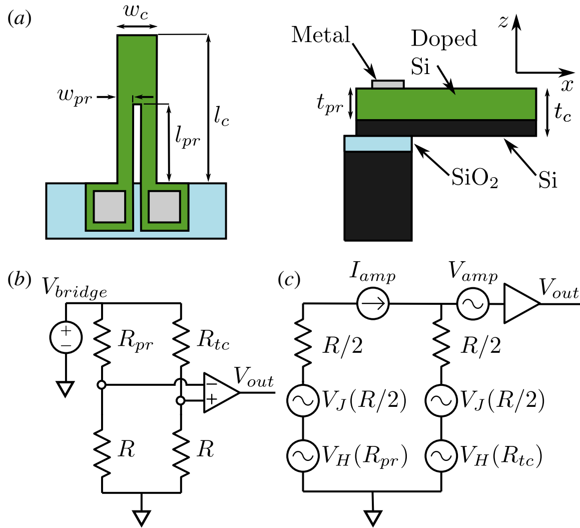

Figure 1. The (*a*) dimensions of the piezoresistive cantilever, (*b*) assumed measurement circuit and (*c*) equivalent noise circuit. The change in resistance of the piezoresistor is transduced with a $1/4$ active Wheatstone bridge, composed of a silicon temperature compensation resistor and two external resistors. The bridge is biased with a voltage source and the differential signal is amplified with an instrumentation amplifier, filtered and recorded.

between the legs is significantly less than the overall width of the cantilever so that the cantilever mechanics are negligibly affected. No stress concentration effects are included, which could potentially enhance the sensitivity [34].

2.1. Measurement circuit

The measurement circuit (figure 1(*b*)) affects both the sensitivity and noise of the system. A $1/4$ active Wheatstone bridge transduces the change in resistance of the piezoresistor, R_{pr}. The bridge is completed with an identical silicon resistor, R_{tc}, for temperature compensation and two external wire-wound resistors, R. A dc voltage, V_{bridge}, biases the Wheatstone bridge. The voltage across the Wheatstone bridge is differentially amplified using an instrumentation amplifier, filtered to set the measurement bandwidth, and measured as V_{out}.

2.2. Sensitivity analysis

The longitudinal stress induced by a point load, F, in a homogeneous linear elastic beam is a function of the distance x from the base and z from the neutral axis of the cantilever:

$$\sigma_l = F\frac{12(l_c - x)z}{w_c t_c^3}. \tag{1}$$

The stress is zero at the neutral axis and varies linearly through the cantilever thickness. The piezoresistive effect transduces the stress into a change in resistance according to

$$\frac{\Delta\rho}{\rho} = \pi_l \sigma_l, \tag{2}$$

where π_l is the longitudinal piezoresistive coefficient. We assume negligible transverse stress in the cantilever legs. This analysis is valid for beams which are long, narrow and thin ($l_c \gg w_c \gg t_c$). A more thorough discussion of the stress, piezoresistive and piezoelectric tensors can be found elsewhere [10, 20, 35].

The piezoresistive coefficient varies with dopant concentration and temperature. We use the recent theoretical model developed by Richter *et al* [36] to calculate the piezoresistive coefficient as $\pi_l = P\pi_0$, where $\pi_0 = 72 \times 10^{-11}\ \text{Pa}^{-1}$ is the longitudinal piezoresistive coefficient at low dopant concentration for a p-type piezoresistor oriented in the $\langle 1\,1\,0\rangle$ direction [35]. The piezoresistance factor, P, accounts for the decrease in piezoresistivity at high dopant concentration and is calculated from the fit presented in [36].

The proportional change in resistance of the piezoresistor for the point load force, F, is

$$\frac{\Delta R}{R} = \frac{6\pi_0\beta^*\gamma(l_c - l_{pr}/2)}{w_c t_c^2}F, \tag{3}$$

where β^* is the efficiency factor of the piezoresistor and γ is a geometry or resistance factor [37]. The efficiency factor accounts for the finite thickness and potentially varying dopant concentration within the piezoresistor, and can be calculated from

$$\beta^* = \frac{2}{t_c}\frac{\int_{-t_c/2}^{t_c/2} q\mu n P z\, \mathrm{d}z}{\int_{-t_c/2}^{t_c/2} q\mu n\, \mathrm{d}z}, \tag{4}$$

where both μ and P vary with n, the dopant concentration.

The resistance factor, γ, accounts for the additional resistance between the electrical contacts that is measured but does not change with applied load, such as conducting traces. These fixed resistances reduce system sensitivity and increase the Johnson noise, so should be minimized. We use $\gamma = 0.9$ as a typical value.

The output from the Wheatstone bridge can be linearized as $\Delta V \approx V_{\text{bridge}}\Delta R/4R$, which is accurate to within 5% for a 10% relative resistance change. The voltage–force sensitivity can then be calculated from

$$S_{FV} = \frac{\Delta V}{\Delta F} = \frac{3\pi_0\beta^*\gamma(l_c - l_{pr}/2)}{2w_c t_c^2}V_{\text{bridge}}. \tag{5}$$

The displacement sensitivity is equal to the product of the force sensitivity and cantilever stiffness, $k = E_c w_c t_c^3/4l_c^3$, yielding

$$S_{XV} = \frac{\Delta V}{\Delta X} = \frac{3E_c\pi_0\beta^*\gamma(l_c - l_p/2)t_c}{8l_c^3}V_{\text{bridge}}, \tag{6}$$

where E_c is the elastic modulus of the cantilever material in the longitudinal direction. The elastic modulus of single crystal silicon varies substantially with crystal orientation, and we use $E_c = 169$ GPa, corresponding to the $\langle 1\,1\,0\rangle$ direction, for all calculations. If the cantilever length is comparable to its width, then plane stress conditions no longer hold. In that case the plate modulus, $E/(1-\nu^2)$, should be substituted for the elastic modulus [38], where ν is the appropriate Poisson's ratio for the material and crystallographic orientation of the beam.

Force sensitivity can be maximized by making the cantilever as long, narrow and thin as possible, while displacement sensitivity can be maximized by making the cantilever as thick and short as possible.

The measurement bandwidth of the cantilever is limited by its mechanical resonance. The first resonant mode of a cantilever can be derived from the Euler–Bernoulli beam equation as $f_0 = \frac{1}{2\pi}\sqrt{k/m_{\mathrm{eff}}}$, where the effective mass is $m_{\mathrm{eff}} = 0.243m$ [38].

2.3. *Piezoresistor noise*

The overall noise of a piezoresistive cantilever can be calculated from the Johnson and $1/f$ (Hooge) noise of the resistor [14], the thermomechanical noise of the cantilever [39] and the amplifier noise.

Johnson noise is the result of the thermal motion of carriers within a resistive element and is independent of frequency [40]. The noise spectral density (units = V Hz$^{-1/2}$) for a single resistor is $\sqrt{4k_bTR}$, where k_b is Boltzmann's constant and T is the temperature. The noise spectral density for the entire Wheatstone bridge is

$$V_J = \sqrt{4k_bTR_{pr}}, \tag{7}$$

assuming that all four resistors in the bridge are matched. This result comes from the fact that V_{bridge} is an ac ground, so the input impedance seen by each amplifier input is $R_{pr}/2$. Thus, the Johnson noise voltage at each input to the amplifier is $\sqrt{2k_bTR_{pr}}$. The noise sources are uncorrelated, so the overall root-mean-square (RMS) noise is $\sqrt{4k_bTR_{pr}}$.

The piezoresistor resistance, R_{pr}, is approximately $2\rho l_{pr}/w_{pr}t_{pr}\gamma$, where ρ is the resistivity of the piezoresistor and γ is the resistance factor introduced earlier. The resistivity varies with dopant concentration according to $\rho = 1/q\mu n$ where q is the single electron charge and μ is the concentration-dependent majority carrier mobility [41].

A critical parameter in the design optimization process is the electrical power dissipated in the piezoresistor, $W = V_{\mathrm{bridge}}^2/4R_{pr}$. Although Joule heating can be used for alternative imaging modes and new functions [42], significant heating can damage the sample or lead to excess piezoresistor noise [15]. In the optimization process, the power dissipation is constrained to 1 mW or less.

The dominant $1/f$ noise source in silicon piezoresistors is Hooge noise [14]. Hooge noise is a fluctuation in resistor conductance which varies inversely with the number of charge carriers in the material [43]. In contrast with Johnson noise, which is a voltage noise, Hooge noise is a conductivity noise and thus depends on the bias voltage. The noise is independent of the resistance and is inversely proportional to the number of carriers in the resistor. The noise spectral density of the Wheatstone bridge is

$$V_H = \sqrt{\frac{\alpha V_{\mathrm{bridge}}^2}{2Nf}}, \tag{8}$$

where the bias across the piezoresistor is $V_{\mathrm{bridge}}/2$, N is the total number of carriers in the resistor and f is the frequency. The $1/f$ noise of the temperature compensation resistor is included in equation (8), which increases the RMS voltage noise by a factor of $\sqrt{2}$. The parameter α is an empirical value that is dependent upon the crystal lattice quality. For epitaxial piezoresistors, $\alpha = 10^{-5}$ has been reported [7]. The number of carriers in the epitaxial piezoresistor is roughly $N = nl_{pr}w_ct_{pr}$, assuming a constant current density.

Table 2. The amplifier noise coefficients. The coefficients can be calculated from the typical performance curves included with most amplifiers.

	INA103	INA116
A_{VJ} (nV Hz$^{-1/2}$)	1.2	28
A_{VF} (nV)	6	300
A_{IJ} (fA Hz$^{-1/2}$)	2000	0.1
A_{IF} (fA)	2500	1

The thermomechanical force spectral density (units = N Hz$^{-1/2}$) imposes a fundamental limit on the MDF and can be calculated for frequencies below the first harmonic mode from $\sqrt{2kk_bT/\pi f_0 Q_M}$, where k, Q_M and f_0 are the spring constant, mechanical quality factor and first resonant mode frequency of the cantilever, respectively [39]. The quality factor varies with cantilever dimensions and ambient conditions, and can be limited by a variety of energy loss mechanisms [44]. Viscous losses dominate in air at atmospheric pressure, and we calculate Q_M using [45]. The quality factor is on the order of 20 for the cantilever dimensions in this work. The equivalent voltage spectral density is

$$V_{TH} = S_{FV}\sqrt{\frac{2kk_bT}{\pi f_0 Q_M}}. \tag{9}$$

Thermomechanical noise is smaller than the device and amplifier noise for the range of designs considered in this work but is included in the model for generality.

The piezoresistor measurement circuit includes an instrumentation amplifier, which contributes additional voltage and current noise. Its noise contribution is

$$V_A = \sqrt{A_{VJ}^2 + \frac{A_{IJ}^2R_{pr}^2}{2} + \frac{1}{f}\left[A_{VF}^2 + \frac{A_{IF}^2R_{pr}^2}{2}\right]}, \tag{10}$$

where A_{VJ} and A_{IJ} describe the input referred Johnson voltage and current noise of the amplifier, while A_{VF} and A_{IF} describe its $1/f$ noise. For example, the voltage and current noise power spectral densities of the amplifier are $A_{VJ}^2 + A_{VF}^2/f$ and $A_{IJ}^2 + A_{IF}^2/f$, respectively. The current noise terms include the input impedance ($R_{pr}/2$) and a factor of 2 to account for the voltage noise induced by the amplifier current noise at each input (figure 1(*c*)). The current noise of the amplifier leads to increased noise from high impedance sensors.

The piezoresistor analysis is performed for the INA103 (Texas Instruments, USA), a high bandwidth commercial instrumentation amplifier. The low voltage noise and high current noise of the INA103 favor the design of a low impedance piezoresistor. In contrast, the high impedance of a typical piezoelectric film necessitates an amplifier with high input impedance, low input bias current and low current noise, and we use the INA116 (Texas Instruments, USA) for the piezoelectric analysis. The amplifier noise coefficients are listed in table 2.

2.4. Force and displacement resolution

The MDF or MDD is typically equated to the RMS force or displacement noise [46]. For example, the force noise spectral density (units = N Hz$^{-1/2}$) is

$$F_V = \frac{\sqrt{V_J^2 + V_H^2 + V_{TH}^2 + V_A^2}}{S_{FV}}, \tag{11}$$

which can be integrated over the measurement bandwidth to find the MDF:

$$\mathrm{MDF} = \sqrt{\int_{\mathrm{f_{min}}}^{\mathrm{f_{max}}} F_V^2 \,\mathrm{d}f}. \tag{12}$$

Calculating the MDF via the frequency-dependent force noise accounts for the potential frequency dependence of both the sensitivity and noise. Sensitivity is independent of frequency for the piezoresistive cantilever, but will vary with frequency for the piezoelectric cantilever. Nonetheless, it is useful to calculate the input referred voltage or charge noise:

$$V_{TOT} = \sqrt{\int_{\mathrm{f_{min}}}^{\mathrm{f_{max}}} \left(V_J^2 + V_H^2 + V_{TH}^2 + V_A^2\right) \mathrm{d}f}. \tag{13}$$

The piezoresistive cantilever design requires a careful balance between several design parameters. For example, increasing the length of the piezoresistor (l_{pr}) increases the Johnson noise and amplifier noise, decreases the $1/f$ noise and power dissipation, but increases the sensitivity. Furthermore, the quality factor and resonant frequency in a fluid such as air or water depend nonlinearly on the cantilever dimensions and determine the thermomechanical noise floor. In the face of this complexity we use a computational design approach [16], but there are numerous references on the analytical piezoresistive cantilever design as well [10, 13–15, 47].

3. Piezoelectric cantilever analysis

For simplified analysis, we assume the piezoelectric film extends the full length and width of the cantilever, l_c and w_c respectively, and has t_{pe} thickness (figure 2(*a*)). We will show later that the length and width assumptions are justified in order to maximize sensitivity and minimize noise, although the model could be extended to handle smaller piezoelectric dimensions. The piezoelectric film is sandwiched between two metal electrodes which collect the generated charge. We assume that the metal films are 50 nm thick sputtered Ti and discuss their impact on sensing resolution later.

In operation, a force or displacement applied to the tip of the cantilever polarizes the piezoelectric film and the resulting charge or voltage is amplified and recorded. The piezoelectric cantilever is modeled as a charge source, Q_{pe}, in parallel with the capacitance ($C_{pe} = \epsilon_r \epsilon_0 l_c w_c / t_{pe}$) and resistance ($R_{pe} = \rho t_{pe} / w_c l_c$) of the film (figure 2(*b*)). Whereas the piezoresistor must continuously dissipate power during operation, the piezoelectric film is an active sensor and only requires an external power source for signal amplification.

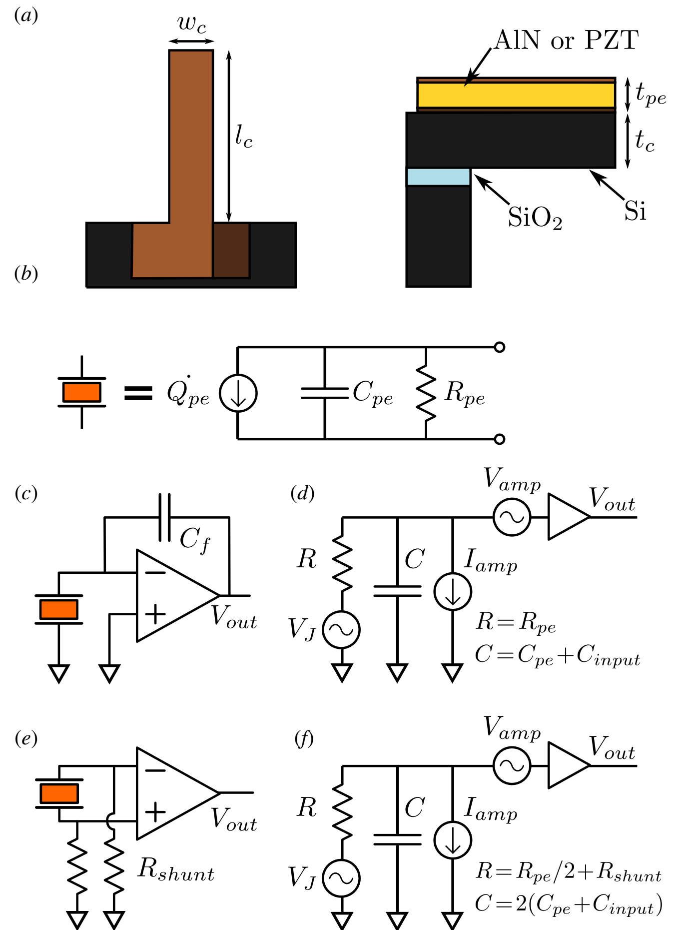

Figure 2. The (*a*) dimensions of the piezoelectric cantilever, (*b*) device circuit model, (*c*) the charge measurement circuit, (*d*) its equivalent noise circuit, (*e*) the voltage measurement circuit and (*f*) its equivalent noise circuit. The film can be represented as a stress-dependent charge generator (Q_{pe}) in parallel with the resistance (R_{pe}) and capacitance (C_{pe}) of the film. The charge measurement circuit shown in (*c*) integrates the piezoelectric charge to generate an output voltage. The differential voltage amplifier circuit shown in (*e*) amplifies the voltage drop across the film induced by the charge. Shunt resistors are required in order to limit the common mode voltage induced by the amplifier input bias current.

3.1. Measurement circuit

There are many possible measurement circuits for the piezoelectric device. Two common configurations are the charge amplifier and the voltage amplifier.

3.1.1. Charge amplifier circuit. The charge amplifier configuration (figure 2(*c*)) connects the piezoelectric to the inverting terminal of an operational amplifier. Negative feedback draws current across the feedback capacitor (C_f) in order to drive the voltage drop across the piezoelectric to zero. The additional charge required to cancel the piezoelectric charge is measured at the output of the operational amplifier, where $V_{\mathrm{out}} = Q/C_f$. A switch in parallel with C_f is used to zero the amplifier output.

Two advantages of this circuit are that (1) both terminals of the piezoelectric are at the same potential so there is

ideally no leakage current, which would otherwise reduce low frequency sensitivity, and (2) V_{out} is insensitive to parasitic input capacitances if C_f is large, so the amplifier can be located far away from the sensor.

Unfortunately, the amplifier will always draw a small input bias current, limiting low frequency sensitivity. Also, the circuit is not well suited for the small quantity of charge generated by a microscale device [8]. For example, a 500 μm long, 5 μm wide and 1 μm thick cantilever coated with 200 nm of AlN would only generate an output voltage of 10 μV in response to a 1 nN force for C_f = 100 pF, so would require another amplifier stage.

An alternative form of the circuit uses two charge integrators and an instrumentation amplifier for common mode rejection and signal amplification [26]. However, we will calculate the noise, sensitivity and resolution for the charge-mode measurement circuit shown in figure 2(*c*) for simplicity. The equivalent circuit for noise analysis is shown in figure 2(*d*). As in the rest of the analysis, all noise and sensitivity calculations will be in terms of amplifier input referred values.

3.1.2. Voltage amplifier circuit. Researchers have noted that microscale piezoelectrics, particularly low relative permittivity materials, are often better suited for voltage sensing because both the charge and capacitance scale with the area [48]. An alternative circuit (figure 2(*e*)) is a differential voltage amplifier. A 500 μm × 5 μm × 1 μm thick cantilever with 200 nm of AlN would generate V_{out} of 1 mV in response to a 1 nN force, which is readily measurable even without amplification.

However, there are two downsides to the voltage amplifier circuit. First, there is now a potential drop across the film so charge will slowly leak across it, reducing low frequency sensitivity. Second, parasitic input capacitance will reduce the voltage generated by the piezoelectric. We will include the differential input capacitance of a typical MOSFET amplifier in the analysis (C_{input} = 0.2 pF) and assume that other parasitics are negligible for simplicity, but care should be taken in circuit and device layout to ensure that this approximation remains valid.

The voltage-sensing circuit requires the addition of shunt resistors, R_{shunt}, to provide a current path to ground for the amplifier input bias currents. Additionally, the differential inputs to the amplifier are coupled by the piezoelectric, which complicates the analysis. We can perform half circuit analysis by applying Miller's theorem [49], which relates a differential impedance to a single ended impedance, to find the half circuit model shown in figure 2(*f*). We will look at the sensitivity and noise for this circuit 2(*f*) in terms of the differential voltage at the amplifier inputs.

3.2. Sensitivity analysis

We follow the multilayered cantilever beam analyses presented in [18] and [50], with further descriptions found in [51] and [52]. The neutral axis of the beam relative to its bottom surface ($z = 0$) is

$$z_n = \frac{\sum_i z_i E_i A_i}{\sum_i E_i A_i}, \tag{14}$$

where z_i, E_i and A_i are the distance from the bottom of the cantilever to the midpoint of the layer, the elastic modulus, and the cross-sectional area of layer *i*, respectively. We will consider a four-layered beam: Si ($i = 1$), a 50 nm thick bottom Ti electrode ($i = 2$), a piezoelectric film ($i = 3$) and a 50 nm thick top Ti electrode ($i = 4$).

The curvature of the beam per unit moment applied at the tip of the cantilever is

$$C_m = \frac{1}{\sum_i E_i (I_i + A_i (z_i - z_n)^2)}, \tag{15}$$

where I_i is the moment of inertia of each layer about its center of area.

A force F applied at the tip of the cantilever induces a moment $M = F(l_c - x)$, where x is the distance from the root of the beam. M varies linearly along the length of the beam, so the average moment is $\bar{M} = Fl_c/2$. The bending stress varies linearly through the thickness of the beam, so the average for each layer is the stress at its center of area, z_i. The average longitudinal bending stress for each layer is then

$$\bar{\sigma_{l,i}} = E_i (z_n - z_i) C_m \bar{M}. \tag{16}$$

The piezoelectric film is polarized by the applied stress and the induced charge is

$$Q = d_{31} \bar{\sigma_{l,i}} w_c l_c, \tag{17}$$

where d_{31} (units = pC N^{-1} = pm V^{-1}) is the transverse piezoelectric coefficient. The amplifier has a small input bias current, on the order of 1 fA for typical MOSFET amplifiers. The effect of the bias current is negligible for the design parameters and measurement frequencies we will consider, but should be included when Q is on the order of the input bias current integrated for the duration of the measurement, e.g. nanoscale cantilevers and sub-Hz frequencies.

The charge sensitivity (units = C/N) can be found by combining equations (16) and (17) to find

$$S_{FQ} = \frac{\Delta Q}{\Delta F} = \frac{1}{2} d_{31} E_{pe} (z_n - z_{pe}) C_m l_c^2 w_c, \tag{18}$$

where $z_n - z_{pe}$ is distance from the neutral axis to the centroid of the piezoelectric film. Note that the charge sensitivity is independent of beam width due to the w_c that can be factored out of the denominator of C_m.

The voltage drop across the piezoelectric per unit charge can be found by analyzing the voltage amplifier half circuit (figure 2(*f*)). The differential voltage (twice the half circuit voltage) to the amplifier can be written as

$$V = \frac{I R_{pe}}{1 + 2\pi f R_{pe} C_{pe}}, \tag{19}$$

where we assume $R_{pe}/2 \parallel R_{shunt} \approx R_{pe}/2$ and $C_{input} << C_{pe}$ for the derivation but use the more general form in all calculations. For best performance R_{shunt} should be larger than R_{pe} (figure 3). A reverse-biased diode can provide a

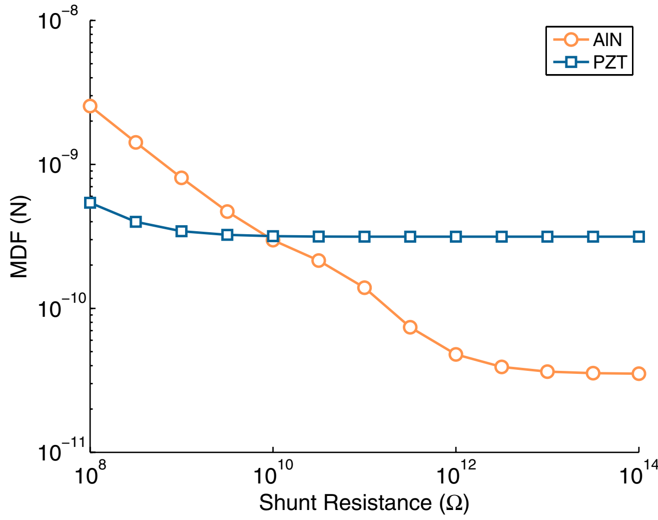

Figure 3. The resolution from the voltage amplifier circuit varies with shunt resistance. Shunt resistance should be maximized in order to increase sensitivity and reduce noise at low frequencies. AlN requires a higher shunt resistance than PZT due to its higher resistivity. The charge amplifier circuit does not require a shunt resistance and is not shown. The force resolution versus shunt resistance is calculated for the example optimized cantilever designs presented in table 6.

higher shunt resistance (e.g. 1 TΩ) than is often possible with resistors [53].

The current flow to ground, I, is $2\pi f Q_{pe}$ assuming that the input offset current of the differential amplifier is small (typically 0.1 fA) relative to the piezoelectric current. As in the charge sensing case, this is a valid assumption except for nanomechanical devices and sub-Hz frequency operation.

The voltage sensitivity can be calculated by combining equations (18) and (19) to find

$$S_{FV} = S_{FQ} \frac{2\pi f R_{pe}}{1 + 2\pi f R_{pe} C_{pe}}. \tag{20}$$

The voltage sensitivity at moderate frequencies ($f > 1/2\pi R_{pe} C_{pe}$) can be simplified to

$$S_{FV} \approx \frac{d_{31}}{2\epsilon_0 \epsilon_r} E_{pe}(z_n - z_{pe}) C_m l_c t_{pe}. \tag{21}$$

The high-pass frequency is $1/2\pi R_{pe}C_{pe} \approx 1/2\pi \rho \epsilon_r \epsilon_0$, which is lower for AlN (0.2 Hz) than PZT (20 Hz). Both the sensitivity and the noise roll off below this characteristic frequency.

The displacement sensitivity is equal to the product of the force sensitivity and cantilever stiffness, $k = 3/C_m l_c^3$, leading to charge–displacement and voltage–displacement sensitivities of

$$S_{XQ} = \frac{3d_{31}}{2l_c} E_{pe}(z_n - z_{pe}) w_c \tag{22}$$

and

$$S_{XV} = \frac{3d_{31}}{2\epsilon_r \epsilon_0 l_c^2} E_{pe}(z_n - z_{pe}) t_{pe}. \tag{23}$$

We emphasize that equations (21) and (23) are approximations and accurate only for frequencies above the high-pass frequency of the piezoelectric. The more general frequency-dependent forms are used in all calculations.

The resonant frequency of the piezoelectric cantilever can be calculated in the same manner as the piezoresistive cantilever.

3.3. Noise analysis

The noise spectral density for a piezoelectric cantilever can be calculated similarly to the piezoresistive cantilever case. For both circuit configurations we will consider Johnson noise of the device, amplifier noise and thermomechanical noise, which are all present at equilibrium. The bias current of the amplifier and piezoelectric current are shot noise sources, and will be discussed at the end of the noise section.

In the case of charge sensing (figure 2(*c*)), the Johnson voltage noise of R_{pe} leads to a voltage drop across C_{pe} (assuming $C_{pe} \gg C_{\text{input}}$) which must be compensated by the feedback circuit, leading to a charge noise spectral density (units = C Hz$^{-1/2}$) of

$$Q_J = \frac{\sqrt{4k_b T R_{pe}} C_{pe}}{1 + 2\pi f R_{pe} C_{pe}}. \tag{24}$$

The low-pass filter action of C_{pe} leads to the noise actually decreasing as R_{pe} is increased.

In addition, the amplifier contributes charge noise of

$$Q_A = \sqrt{A_{VJ}^2 C_{pe}^2 + \frac{A_{VF}^2 C_{pe}^2}{f} + \left(\frac{A_{IJ}}{2\pi f}\right)^2 + \frac{1}{f}\left(\frac{A_{IF}}{2\pi f}\right)^2}, \tag{25}$$

where the amplifier voltage noise directly induces charge noise while the amplifier current noise is integrated to find the equivalent charge. The amplifier noise coefficient syntax is identical to the piezoresistor case.

The thermomechanical charge noise, Q_{TH}, can be calculated by substituting S_{FQ} (equation (18)) into equation (9).

In the voltage amplifier case (figure 2(*f*)), the Johnson voltage noise of $R_{pe}/2 \parallel R_{\text{shunt}}$ is low-pass filtered by $2C_{pe} \parallel 2C_{\text{input}}$. For brevity we will again assume that $R_{\text{shunt}} \gg R_{pe}/2$ and $C_{pe} \gg C_{\text{input}}$, but use the more general form in all calculations. The voltage spectral density at the amplifier input is

$$V_J = \frac{\sqrt{4k_b T R_{pe}}}{1 + 2\pi f R_{pe} C_{pe}}. \tag{26}$$

A factor of $\sqrt{2}$ is included to account for both amplifier inputs in the full circuit (figure 2(*e*)).

The current and voltage noise of the amplifier contribute differential voltage noise of

$$V_A = \sqrt{(A_{VJ}^2 + 2A_{IJ}^2 Z^2) + \frac{1}{f}(A_{VF}^2 + 2A_{IF}^2 Z^2)}, \tag{27}$$

where Z is the impedance seen by the amplifier at its inputs. The current noise terms include a factor of 2 to account for the noise at both amplifier inputs (figure 2(*f*)). For both piezoelectric circuits we use the amplifier noise coefficients of the INA116, a MOSFET instrumentation amplifier with low current noise (table 2).

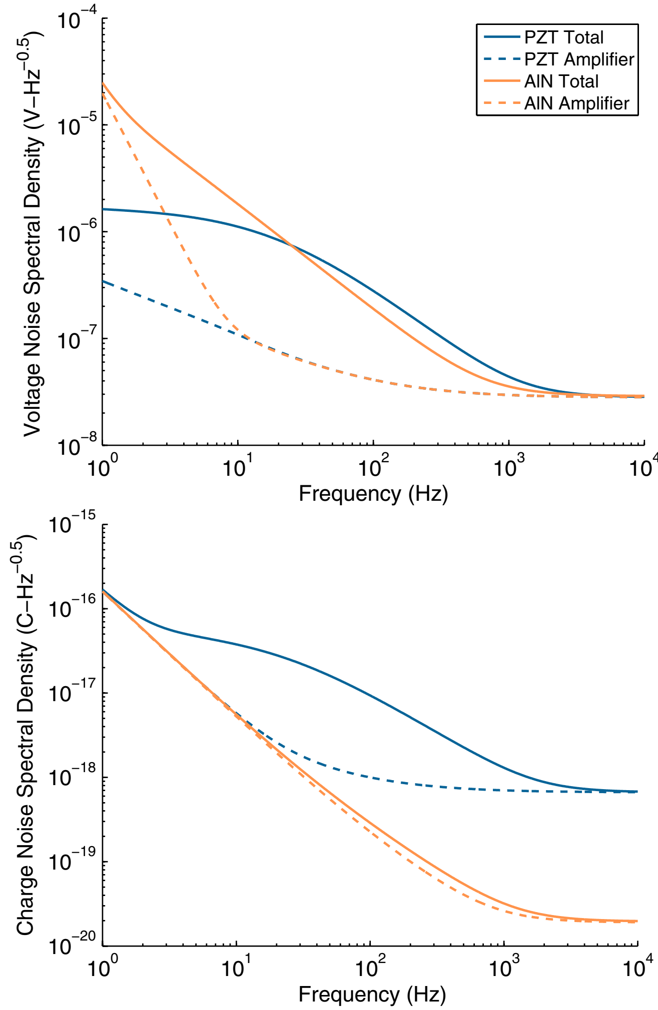

Figure 4. Calculated noise spectra for the optimized example piezoelectric cantilevers in table 6. (*a*) Voltage noise is dominated by the Johnson noise of the device at moderate frequencies and the amplifier voltage noise at high frequency. The PZT Johnson noise rolls off at low frequency due to its relatively small $R_{pe}C_{pe}$ product compared to AlN. The increase in AlN amplifier noise at low frequency is due to its current noise and the relatively small capacitance of the AlN film. (*b*) The charge noise is limited by amplifier voltage noise at high frequency. AlN, with a lower permittivity than PZT, has a correspondingly lower charge noise. At moderate frequencies, the AlN noise spectrum is limited by the amplifier while PZT is limited by the device Johnson noise.

The thermomechanical voltage noise, V_{TH}, can be calculated from equations (20) and (9) in the same manner as previously described for the thermomechanical charge noise.

The voltage and charge noise spectra for the example cantilevers in table 6 are plotted in figure 4. Both the amplifier noise and overall noise are plotted to illustrate the frequencies where noise is limited by the amplifier or by the device.

Shot noise due to the amplifier bias current and transduced piezoelectric current need to be considered for both measurement circuits. While the bias current of the amplifier is a shot noise source, the overall amplifier current noise is a much larger noise source, which can be confirmed from the amplifier specifications. We have included the current noise of the amplifier in analyzing both amplifier circuits, so the amplifier shot noise is accounted for.

Table 3. Summary of the relationship between design parameters and the force sensitivity (S_{FQ} or S_{FV}), displacement sensitivity (S_{XQ} or S_{XV}), Johnson and amplifier charge noise (Q_J and Q_A), Johnson and amplifier voltage noise (V_J and V_A) for a piezoelectric cantilever. As the design parameter increases with all other parameters held constant, the measurand either increases (↑), decreases (↓), can increase or decrease depending on other design parameters (↕) or does not change appreciably (–).

	S_{FQ}	S_{XQ}	Q_J	Q_A	S_{FV}	S_{XV}	V_J	V_A
l_c (m)	↑	↓	↑	↑	↑	↓	↓	↓
w_c (m)	–	↑	↑	↑	↓	–	↓	↓
t_c (m)	↕	↕	–	–	↕	↕	–	–
t_{pe} (m)	↕	↕	↓	↓	↕	↕	↑	↑
ϵ_r (–)	–	–	–	↑	↓	↓	↓	↓
ρ (Ω cm)	–	–	↓	–	↑	↑	↓	–
d_{31} (pC N^{-1})	↑	↑	–	–	↑	↑	–	–
E_{pe} (Pa)	↕	↕	–	–	↕	↕	–	–

The current transduced by the piezoelectric element is another shot noise source. However the transduced current depends on the spectral content and amplitude of the mechanical signal being measured, in contrast with the rest of the noise analysis. Additionally, the shot noise scales as the square root of the signal ($\sqrt{2qI}$), meaning that if the shot noise generated by the minimum detectable signal does not change the noise spectrum then shot noise can be safely ignored. We calculated the shot noise for a resolution limited, broadband force signal and found the integrated shot noise consistently to be at least an order of magnitude smaller than the other intrinsic noise sources. In summary, shot noise can be safely ignored for the range of device dimensions and frequencies investigated here.

3.4. Force and displacement resolution

We calculate the overall force and displacement noise in the same fashion as discussed for the piezoresistive cantilever. For example, the force noise spectral density (units = N Hz$^{-1/2}$) for the two measurement circuits are

$$F_Q = \frac{\sqrt{Q_J^2 + Q_{TH}^2 + Q_A^2}}{S_{FQ}} \tag{28}$$

and

$$F_V = \frac{\sqrt{V_J^2 + V_{TH}^2 + V_A^2}}{S_{FV}}. \tag{29}$$

The MDF can then be found by integrating the force noise from $f_{\min}$ to $f_{\max}$. The same calculations can be carried out to calculate the displacement noise spectral density and MDD.

There is significantly less literature on the design of piezoelectric cantilevers than their piezoresistive counterparts, so we have summarized the impact of the cantilever design parameters on piezoelectric sensitivity and noise in table 3.

Using the case of voltage-force sensing as an example, increasing l_c increases the sensitivity while reducing the noise, so l_c should be maximized. Increasing the width, w_c, reduces the sensitivity faster than it reduces the noise, so the cantilever

Table 4. Summary of the standard optimization constraints that are enforced.

Parameter constraints	Nonlinear constraints
$t_c \geqslant 1\mu$m	$f_0 \geqslant 2 f_{\max}$
$w_c \geqslant 5t_c$	$W \leqslant 1$ mW
$l_c \geqslant 5w_c$	
$V_{\text{bridge}} \leqslant 10$ V	
$n \leqslant 4.4 \times 10^{19}$ cm^{-3}	
$t_{pe} \geqslant 200$ nm	
$R_{\text{shunt}} \leqslant 1$ TΩ	

width should be minimized. However, if the piezoelectric becomes narrower than the cantilever, the sensitivity remains constant while the noise increases, so a piezoelectric film that covers the entire top surface of the cantilever is preferable. The impact of cantilever and piezoelectric thickness depends on their ratio and the material properties of the cantilever, but in general they should both be minimized in order to maximize sensitivity and minimize the noise. Increasing the permittivity, ϵ_r, linearly reduces the sensitivity and the device Johnson noise but does not affect the amplifier voltage noise, and the net effect is that the permittivity should be minimized. Increasing the resistivity leads to increased sensitivity and reduced noise, so the resistivity should be maximized. Finally, d_{31} only affects the sensitivity so should be maximized. This analysis can be extended to displacement or charge sensing as well.

4. Design and optimization methods

Analytically optimizing the design of the two cantilever models introduced would be quite involved due to their complexity. Numerical optimization methods are available which only require that the user provides a function to compute the optimization target (e.g. force resolution) from a set of design parameters. We have previously applied numerical optimization to the design of piezoresistive cantilevers with arbitrary dopant profiles [16] and will apply the same technique here.

For a typical design problem, a measure of performance should be minimized given a set of design parameter bounds, nonlinear parameter constraints and fixed measurement conditions, such as $f_{\min}$ and $f_{\max}$. The designer provides an initial design guess to the optimization routine, which then iteratively computes search directions and step lengths. We use the interior-point method with the gradient approximated by finite-differences and quasi-Newton Hessian updates as implemented by fmincon in Matlab (Mathworks, Cambridge, MA). Optimization typically takes less than a minute for the analysis models presented in this work. Although the problem is not strictly convex, the global optimum can reliably be found by starting from many random initial guesses until multiple iterations converge to within a small tolerance.

Unless otherwise noted in the text we will use $f_{\min} =$ 1 Hz, $f_{\max} = 10$ kHz and the constraints listed in table 4. We consider three cantilever types: p-type (boron) piezoresistors and both AlN and PZT piezoelectrics. The constraint on t_{pe} is based upon the reduction in piezoelectric coefficients for thin piezoelectric films, to be discussed in the next paragraph, while the constraint on n is based on the solid solubility of boron in silicon at 800 °C [54].

The mechanical, electrical and piezoelectric material properties used in all design calculations are summarized in table 5. Piezoelectric properties vary enormously with deposition technique, substrate lattice constant, film thickness and composition [20], so we have surveyed experimental data in the literature to find the range of typical values.

AlN is most commonly deposited using reactive sputtering, and although its transverse piezoelectric coefficient varies with thickness [60–63] its other properties do not vary significantly. However, PZT is often deposited using either sol–gel processing or sputtering, and its properties vary more significantly. For example, the relative permittivity (ϵ_r) of sol–gel deposited PZT can vary from 200 [70] to 1300 [71], while the magnitude of the transverse piezoelectric coefficient (d_{31}) ranges from 35–70 pC N^{-1} for sol–gel PZT [30, 68] to 60–100 pC N^{-1} for sputtered PZT [65, 66, 68] to 130 pC N^{-1} for epitaxial PZT [55]. The piezoelectric properties degrade for thin AlN or PZT films, so we constraint $t_{pe} \geqslant 200$ nm. We only consider thin piezoelectric films in this work (<1 μm), so assume that the transverse piezoelectric coefficient is roughly independent of thickness for the 200–1000 nm thickness range.

The optimization and modeling code is an open source and freely available (appendix A), so can be used to analyze particular cases in more detail.

5. Results and discussion

In this section, we design optimized cantilevers for a variety of conditions and constraints. For compactness, we only plot the cantilever performance (e.g. MDF) but provide detailed design parameters in table 6 for the case of cantilevers optimized for force sensing with $f_{\min} = 1$ Hz, $f_{\max} = 10$ kHz and the standard set of constraints presented in table 4.

5.1. Choice of piezoelectric material and sensing circuit

Several choices need to be made in designing a piezoelectric cantilever sensor. In addition to the sensor geometry, the material and measurement circuit need to be selected. Before comparing the piezoelectric and piezoresistive cantilevers we will examine the relative merits of charge and voltage sensing (figure 2) to limit the number of comparisons needed in the next subsection.

Figure 5 compares the optimal force resolution attainable with each combination of piezoelectric material and circuit for a given value of $f_{\max}$. For PZT, a lower MDF is possible with charge sensing than with voltage sensing. The converse is true for AlN. The resolution of voltage AlN is roughly two times better than charge PZT for the assumed design constraints and material properties. However, this may change depending on the specific details of the application. Based upon these results, we will assume voltage sensing for the AlN devices and charge sensing for the PZT devices in the remainder of the paper.

Table 5. Material property ranges assumed for the design analysis. The mechanical and electrical properties of the piezoelectric films are thickness and processing dependent. Typical values for ≈ 500 nm thick sputtered AlN and sputtered or sol–gel PZT films are used. Higher piezoelectric coefficient films such as epitaxial PZT with $d_{31} = 130$ pC N^{-1} [55] have been demonstrated but are not widely available. The Si elastic modulus is based upon a ⟨1 1 0⟩ cantilever orientation.

Material	E (GPa)	ρ (kg m^{-3})	d_{31} (pC N^{-1})	ϵ_r (–)	ρ (Ω-cm)
Si	169 [56]	2330	–	–	–
Ti	90 [57]	4500	–	–	–
AlN	396 ± 40 [58–60]	3260 [11]	2.2 ± 0.5 [60–63]	10.2 ± 0.5 [59, 62, 64]	10^{12} [62]
PZT	55 ± 20 [30, 55, 65, 66]	7550 [30]	70 ± 30 [30, 55, 65–68]	900 ± 300 [67, 69–71]	10^{8} [72]

Table 6. Example optimized piezoelectric and piezoresistor designs. All three are optimized for force sensing but the AlN device is optimized to use voltage sensing while the PZT device is optimized for charge sensing.

	PR	AlN	PZT
$f_{\min}$ (Hz)	1	1	1
$f_{\max}$ (kHz)	10	10	10
f_0 (kHz)	20	20	20
l_c (μm)	262	307	252
w_c (μm)	5	5	5
t_c (μm)	1	1	1
k (mN m^{-1})	11.7	20.2	28.8
Q_M	13.4	13.2	13.3
l_{pr} (μm)	35	–	–
V_{bridge} (V)	3.8	–	–
t_{pr} (nm)	224	–	–
n (cm^{-3})	4.4×10^{19}	–	–
R (kΩ)	3.6	–	–
W (mW)	1	–	–
t_{pe} (nm)	–	200	420
R_{pe} (Ω)	–	1.3×10^{12}	3.4×10^{8}
C_{pe} (pF)	–	0.7	23.7
S_{FV} at 1 kHz (V mN^{-1})	74.4	465	104
V_{tot} (μV)	1.0	19.8	7.8
MDF (pN)	13.8	47.9	317
MDD (nm)	1.2	2.4	11.0
S_{FQ} at 1 kHz (nC N^{-1})	–	409	2540
Q_{tot} (aC)	–	115	278
MDF (pN)	–	281	109
MDD (nm)	–	13.9	3.8

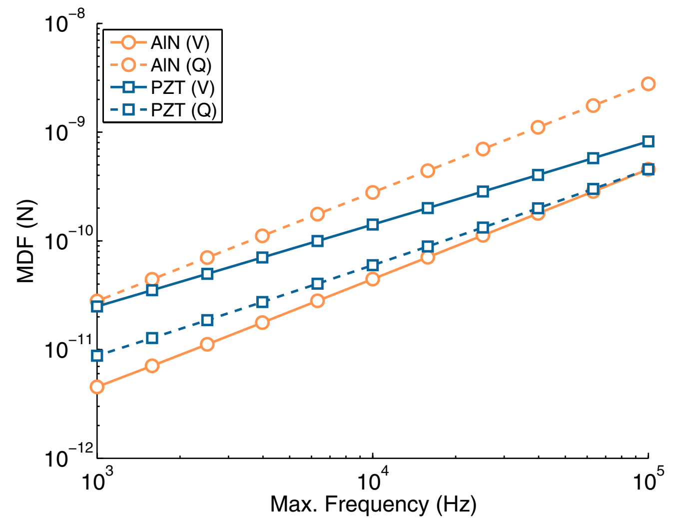

Figure 5. A comparison between the optimal force resolution of AlN and PZT piezoelectric cantilevers using charge sensing or voltage sensing circuits. For each value of $f_{\max}$ the cantilever is optimized for force sensing within the standard design constraints. Charge measurement is preferred for PZT while voltage readout is preferred for AlN.

While the d_{31} of PZT is significantly higher than that of AlN, its voltage sensitivity suffers due to its high permittivity and low resistivity. Charge sensitivity does not depend on these parameters, although charge noise does, so PZT performs significantly better with charge sensing than voltage sensing. The voltage-sensing performance of AlN is partly explained by its low permittivity and high resistivity, but another factor is its high elastic modulus.

5.2. Elastic modulus and maximizing force sensitivity

The elastic moduli of the piezoelectric film and cantilever beam play large roles in determining the optimal layer thicknesses (equation (21)). For example, increasing the elastic modulus of the piezoelectric film can increase sensitivity, but only if the film thickness and cantilever thickness are chosen appropriately. Otherwise, increasing E_{pe} reduces the normalized moment (equation (15)) and shifts the neutral axis toward the film's centroid (equation (14)), which may lead to a reduction in sensitivity despite the apparent linear dependence of sensitivity on E_{pe}. Additionally, a thicker piezoelectric film is favored for voltage sensing in order to minimize the film capacitance.

The sensitivity is difficult to intuitively maximize. However, the analysis can be simplified by non-dimensionalizing the sensitivity in terms of the thickness and elastic modulus ratios of the piezoelectric film to the silicon beam, t_{pe}/t_c and E_{pe}/E_c. The optimal film thickness ratio for a given elastic modulus ratio can then be computed, as shown in figure 6. As the modulus of the piezoelectric increases, its thickness should be reduced relative to the beam thickness. The stiffer the piezoelectric film is relative to the cantilever, the greater the potential sensitivity. Similar results hold for charge-force sensing, except an even thinner film is favored because its capacitance does not affect its charge sensitivity.

The displacement sensitivity is more difficult to treat analytically because the overall beam stiffness needs to be constrained. For example, absent any stiffness constraint the thickness ratio diverges and the ideal voltage–displacement sensor would have the thickest possible piezoelectric film (equation (23)).

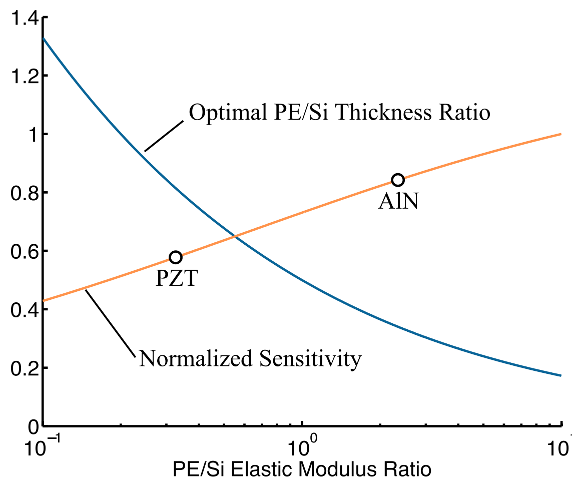

Figure 6. Non-dimensional sensitivity analysis for piezoelectric force sensing using voltage readout. The optimal ratio of the piezoelectric film thickness to the underlying silicon beam depends on the ratio of their elastic moduli. For example, as the piezoelectric becomes stiffer, its thickness should be reduced to ideally position the beam's neutral axis. If the piezoelectric film thickness is chosen appropriately, force sensitivity improves as the elastic modulus of the piezoelectric increases. We assume that the silicon beam is oriented in the ⟨1 1 0⟩ direction and use $E_c = 169$ GPa.

The results illustrate one aspect of the reason for AlN's good sensing performance despite its low transverse piezoelectric coefficient. More generally, resolution is determined by both the sensitivity and noise. In this work, we primarily focus on the case where the extrinsic ambient noise (e.g. vibrations, electromagnetic interference) is much less than the intrinsic device and circuit noise. However, if the ambient noise floor is larger than the intrinsic noise, then resolution optimization and sensitivity maximization will lead to the same design.

5.3. Uncertainty in piezoelectric material properties

The material properties of the piezoelectric film can vary significantly, affecting cantilever performance. However, standard uncertainty analysis methods are difficult to apply to the analysis model due to its complexity. In order to assess the impact of material variability, we first generated optimized cantilever designs for force sensing using the nominal material properties in table 5 and the standard optimization constraints in table 4, corresponding to the designs in table 6. We then calculated the MDF for the range of material properties reported in the literature using the Monte Carlo method ($N = 10\,000$) and assuming independent, uniform distributions of the the piezoelectric elastic modulus (E), transverse piezoelectric coefficient (d_{31}) and relative permittivity (ϵ_r) within the bounds noted in table 5.

The resulting probability density functions are shown in figure 7. The MDF standard deviations are 13% and 30% of the mean MDF for AlN and PZT, respectively. The magnitude of the variation is primarily due to uncertainty in d_{31} while the distributions are skewed due to uncertainty in E, with ϵ_r playing a minor role. The MDF variance could be reduced significantly in practice by measuring the relevant properties for a particular process and then designing the cantilever accordingly.

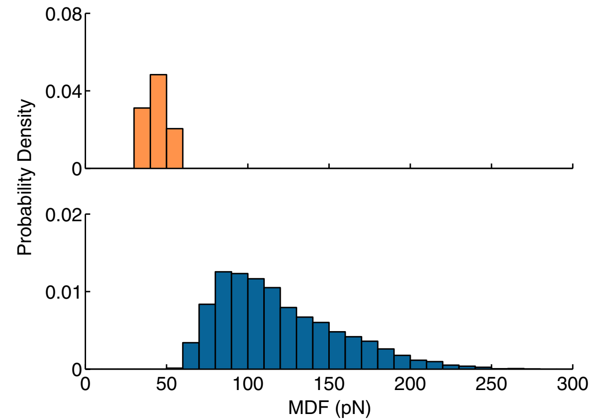

Figure 7. Probability density functions of the minimum detectable force (MDF) for AlN (top) and PZT (bottom) using the Monte Carlo method assuming that the material properties of the piezoelectric films vary independently and uniformly within the assumed ranges.

The remainder of the paper uses the nominal material properties from table 5. However, the designer should keep in mind that the piezoelectric resolution results can vary up to 30%, independent of the geometric tolerances which affect PE and PR sensing alike.

5.4. Comparing piezoresistive and piezoelectric sensing

We now compare the resolution limits of piezoresistive and piezoelectric sensing. The force noise spectral density and integrated force noise for the optimized cantilevers of table 6 are shown in figure 8. The piezoresistive cantilever has a slight performance advantage, mainly due to its smaller low frequency force noise. The low frequency force noise is limited by $1/f$ noise in the piezoresistor case and Johnson noise for the piezoelectric cantilevers.

However, the cantilever designs in figure 8 are only optimized for a single value of $f_{\max}$ and a single piezoresistor power dissipation ($\leqslant$1 mW). While this a reasonable value for many applications, certain measurements may require less power dissipation, such as a cryostat with fixed power dissipation limits or when probing a temperature sensitive biological sample.

In power constrained applications the performance advantage of piezoresistive sensing declines. Figure 9 compares the optimized MDF for piezoresistor power dissipations of 1 mW and 1 μW with AlN and PZT cantilevers as $f_{\max}$ is varied. For each value of $f_{\max}$, the cantilever design is optimized to minimize the MDF while satisfying the optimization constraints, including the ever increasing f_0 constraint. For a power dissipation of 1 μW, both AlN and PZT cantilevers are preferable to piezoresistive sensing.

The majority of scanning probes are used to measure displacement rather than force. While force sensing cantilevers should be as soft as possible while meeting the minimum resonant frequency requirement, displacement

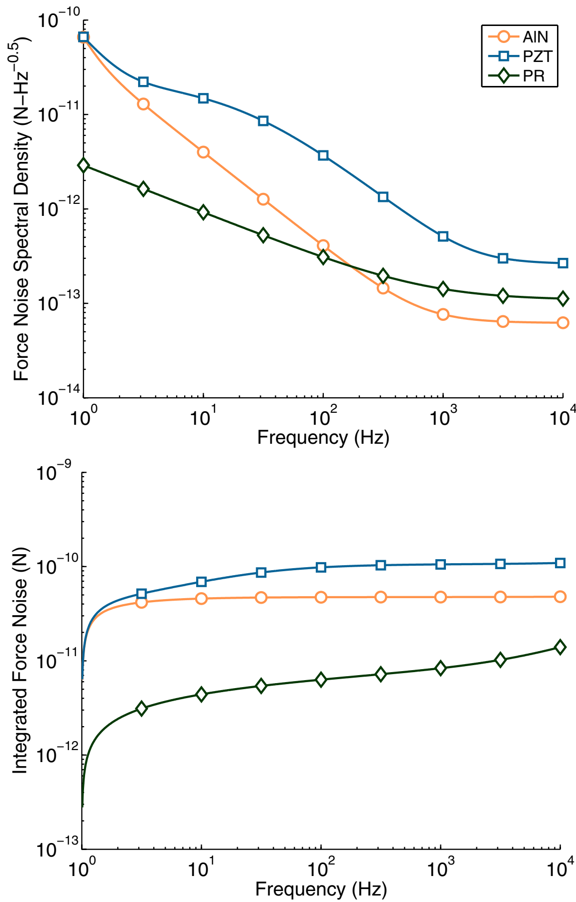

Figure 8. A comparison of (*a*) the force noise spectral density and (*b*) integrated force noise between AlN, PZT and PR cantilever optimized for a measurement bandwidth of 1 Hz to 10 kHz ($f_0 = 20$ kHz). The standard optimization constraints are enforced (table 4), namely a 1 μm thick silicon beam and a maximum piezoresistor power dissipation of 1 mW. The thermomechanical force noise spectral density for the cantilevers is roughly 10 fN Hz$^{-0.5}$.

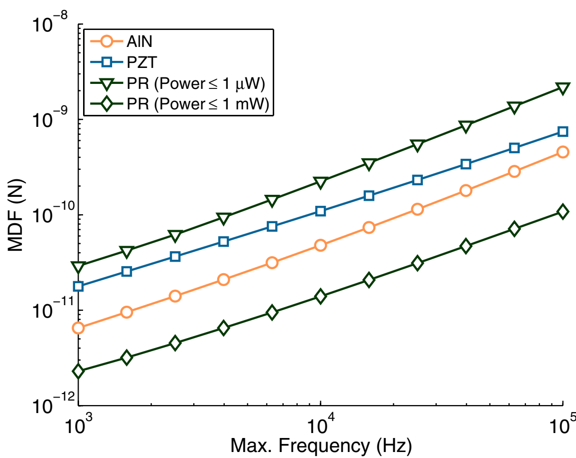

Figure 9. Minimum detectable force for optimized cantilever designs operating from 1 Hz to a varying maximum frequency. The standard optimization constraints are enforced besides the variation in $f_{\max}$ and f_0. Piezoelectric detection becomes preferable to piezoresistive sensing as the maximum power dissipation decreases. The details of the $f_{\max} = 10$ kHz designs are presented in table 6.

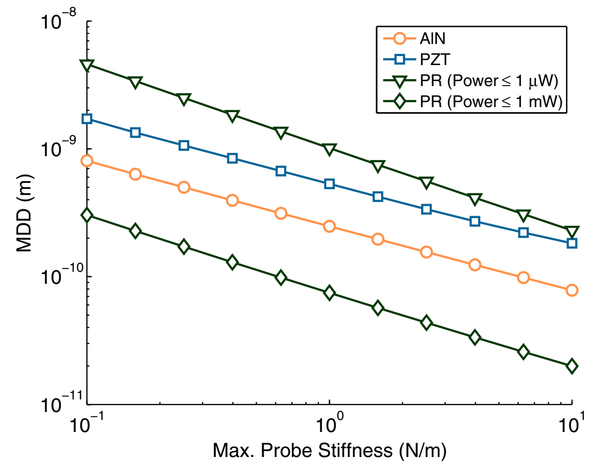

Figure 10. Minimum detectable displacement for optimized cantilever designs with varying maximum stiffness. The standard optimization constraints are used, including a measurement bandwidth of 1 Hz to 10 kHz ($f_0 \geqslant 20$ kHz). All four cantilever types are capable of sub-nm resolution for the given constraints, and are capable of sub-angstrom resolution for smaller measurement bandwidths.

sensing cantilevers should be made as stiff as possible, making the resonant frequency constraint irrelevant. Rather than being constrained by their resonant frequency, cantilevers optimized for displacement resolution are limited by their maximum allowed stiffness because an excessively high stiffness can damage the tip of the probe or the sample.

Figure 10 compares the optimized displacement resolution for the cantilevers as the maximum allowed probe stiffness is varied. The relative performance of the four options is the same as in the force optimization case. While the force and displacement resolutions of both sensing techniques depend on the specific measurement and design constraints, both can have significantly better performance than previous reports suggest [12].

Although piezoresistive sensing generally outperforms piezoelectric sensing (depending on the power dissipation) for the design constraints used so far, we have only examined a single thickness constraint, $t_c \geqslant 1$ μm. However, a minimum or maximum cantilever thickness may be set by a design or fabrication constraint.

As the minimum thickness constraint increases, piezoelectricity becomes the preferred transduction mechanism if the piezoresistor power dissipation remains constant (figure 11). For cantilever beams thicker than 5 μm, AlN has a smaller MDF than the 1 mW piezoresistor, while both PZT and AlN perform better than the 1 μW piezoresistor. Piezoelectric cantilever performance plateaus and even degrades slightly for thin cantilevers due to the difficulty in fabricating thin films with good piezoelectric properties ($t_{pe} \geqslant 200$ nm). The PZT resolution degrades less than the AlN case due to its lower elastic modulus. Thin piezoresistors (<50 nm thick) can be fabricated using epitaxy or diffusion [7], so are preferable to piezoelectric sensing for sub-micron thick cantilevers, at least at the present time.

The finite thickness (50 nm) of the piezoelectric metal electrodes degrades the attainable force resolution because it

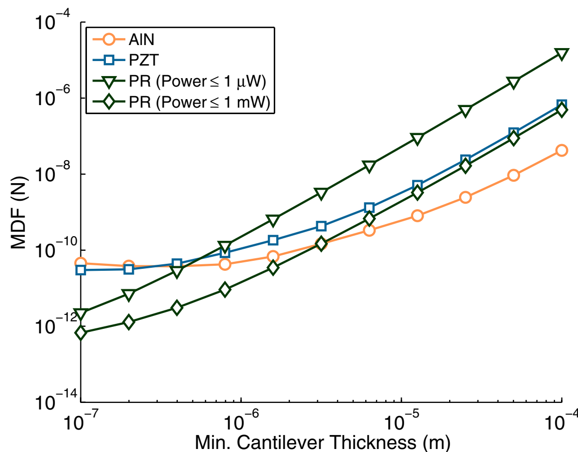

Figure 11. Minimum detectable force for optimized cantilever designs with varying minimum silicon beam thickness. The standard optimization constraints are used, including a measurement bandwidth of 1 Hz to 10 kHz ($f_0 \geqslant 20$ kHz). Piezoelectricity becomes the preferred sensing mechanism as the beam thickness increases assuming that the piezoresistor power dissipation remains constant as the device dimensions scale.

increases the beam stiffness and shifts the neutral axis. The increase in MDF ranges from 10 to 35% for AlN deposited on silicon beams between 100 nm and 1 μm in thickness, while it ranges from 15 to 250% in the PZT case. The reduction is greater for PZT due to its low elastic modulus. On the other hand, the metal electrode thickness slightly improves the displacement resolution very slightly, <5%.

5.5. Comparison with optical detection

We can also compare piezoresistive and piezoelectric sensing with optical detection, which is fundamentally limited by thermomechanical noise [73]. The example cantilever designs in table 6 have MDFs of which range from 14 to 109 pN. In comparison, the thermomechanical noise floor for the cantilevers in the same measurement bandwidth is about 1 pN, excluding the effects of piezoresistor or laser induced self-heating. Thus, for the cantilever designs in table 6, optical sensing could be an order of magnitude better than electronic sensing. However, the gap between the two varies with the design constraints. For example, the 100 nm thick, 1 mW PR cantilever in figure 11 has a MDF only a factor of two greater than its thermomechanical noise limit. While piezoresistive and piezoelectric cantilevers can approach their thermomechanical noise floor, their additional device and amplifier noise makes it difficult to reach. However, they can be made much smaller and softer than their optical counterparts [74], which are limited by a finite laser spot size, enabling a lower thermomechanical force noise floor (equation (9)) and the potential for superior force resolution.

6. Conclusions

We have presented analytical models for the sensitivity and noise of piezoresistive and piezoelectric cantilevers. The models were used to optimize the design of each transducer type and compare their performance characteristics. Piezoresistive sensing is preferred when electrical power dissipation is not an issue, or when the cantilever thickness can be reduced to the nanoscale. Piezoelectric sensing is preferred for thick beams where low power dissipation is required. We surveyed the reported PZT and AlN material properties in the literature and used the Monte Carlo method to examine their impact on cantilever resolution, which can be up to 30% independent of geometric tolerances. In general, piezoresistive sensing has lower noise and lower sensitivity than piezoelectric sensing, making piezoelectricity preferred for measurements with high ambient noise levels. Both cantilever types can operate near the thermomechanical noise resolution limit with proper design.

Both transduction mechanisms are capable of nanoscale force and topography imaging, and the preferred option for a given application will depend on the specific fabrication and operating constraints. Although we have focused on contact mode scanning probes, the same models and optimization methods could be applied to optimize probes for dynamic scanning modes by defining appropriate resonant frequency and measurement bandwidth constraints.

Acknowledgments

This work was supported by the National Institutes of Health under grant EB006745, the National Science Foundation (NSF) under CAREER Award ECS-0449400 and COINS NSF-NSEC ECS-0425914, and a DARPA Young Faculty Award DARPA YFA N66001-09-1-2089. JCD was supported in part by National Defense Science and Engineering Graduate (NDSEG) and NSF Graduate Research fellowships. The authors are grateful to AJ Rastegar and S-J Park for helpful discussions.

Appendix A. Optimization code

The cantilever optimization code is open source and freely available at http://microsystems.stanford.edu/piezoD. It requires Matlab R2008a or newer and the optimization toolbox.

References

[1] Binnig G, Quate C F and Gerber C 1986 Atomic force microscope *Phys. Rev. Lett.* **56** 930

[2] Blanc N, Brugger J, de Rooij N F and Durig U 1996 Scanning force microscopy in the dynamic mode using microfabricated capacitive sensors *J. Vac. Sci. Technol.* B **14** 901

[3] Miller S A, Turner K L and MacDonald N C 1997 Microelectromechanical scanning probe instruments for array architectures *Rev. Sci. Instrum.* **68** 4155

[4] Binnig G, Despont M, Drechsler U, Häberle W, Lutwyche M, Vettiger P, Mamin H J, Chui B W and Kenny T W 1999 Ultrahigh-density atomic force microscopy data storage with erase capability *Appl. Phys. Lett.* **74** 1329

[5] King W P, Kenny T W and Goodson K E 2004 Comparison of thermal and piezoresistive sensing approaches for atomic force microscopy topography measurements *Appl. Phys. Lett.* **85** 2086

[6] Tortonese M 1993 Force sensors for scanning probe microscopy *PhD Dissertation* Stanford University

[7] Harley J and Kenny T 1999 High-sensitivity piezoresistive cantilevers under 1000 angstroms thick *Appl. Phys. Lett.* **75** 289

[8] Tansock J and Williams C 1992 Force measurement with a piezoelectric cantilever in a scanning force microscope *Ultramicroscopy* **42–44** 1464

[9] Itoh T and Suga T 1994 Piezoelectric force sensor for scanning force microscopy *Sensors Actuators A* **43** 305

[10] Barlian A A, Park W T, Mallon J R, Rastegar A J and Pruitt B L 2009 Semiconductor piezoresistance for microsystems *Proc. IEEE* **97** 513

[11] Tadigadapa S and Mateti K 2009 Piezoelectric MEMS sensors: state-of-the-art and perspectives *Meas. Sci. Technol.* **20** 092001

[12] Bell D J, Lu T J, Fleck N A and Spearing S M 2005 MEMS actuators and sensors: observations on their performance and selection for purpose *J. Micromech. Microeng.* **15** S153

[13] Yu X, Thaysen J, Hansen O and Boisen A 2002 Optimization of sensitivity and noise in piezoresistive cantilevers *J. Appl. Phys.* **92** 6296

[14] Harley J and Kenny T 2000 $1/f$ noise considerations for the design and process optimization of piezoresistive cantilevers *J. Microelectromech. Syst.* **9** 226

[15] Park S J, Doll J C, Rastegar A J and Pruitt B L 2010 Piezoresistive cantilever performance: part II. Optimization *J. Microelectromech. Syst.* **19** 149

[16] Doll J C, Park S J and Pruitt B L 2009 Design optimization of piezoresistive cantilevers for force sensing in air and water *J. Appl. Phys.* **106** 064310

[17] DeVoe D and Pisano A 1997 Modeling and optimal design of piezoelectric cantilevermicroactuators *J. Microelectromech. Syst.* **6** 266

[18] Weinberg M 1999 Working equations for piezoelectric actuators and sensors *J. Microelectromech. Syst.* **8** 529

[19] Muralt P 2000 Ferroelectric thin films for micro-sensors and actuators: a review *J. Micromech. Microeng.* **10** 136

[20] Trolier-McKinstry S and Muralt P 2004 Thin film piezoelectrics for MEMS *J. Electroceramics* **12** 7

[21] Tabib-Azar M and Garcia-Valenzuela A 1995 Sensing means and sensor shells: a new method of comparative study of piezoelectric, piezoresistive, electrostatic, magnetic, and optical sensors *Sensors Actuators A* **48** 87

[22] Wang Q-M, Du X-H, Xu B and Cross L E 1999 Theoretical analysis of the sensor effect of cantilever piezoelectric benders *J. Appl. Phys.* **85** 1702

[23] Kursu O, Kruusing A, Pudas M and Rahkonen T 2009 Piezoelectric bimorph charge mode force sensor *Sensors Actuators A* **153** 42

[24] Itoh T and Suga T 1995 Minimum detectable force gradients of piezoelectric microcantilever *J. Micromech. Microeng.* **5** 231

[25] Minne S, Manalis S and Quate C 1995 Parallel atomic force microscopy using cantilevers with integrated piezoresistive sensors and integrated piezoelectric actuators *Appl. Phys. Lett.* **67** 3918

[26] Chu J, Maeda R, Itoh T and Suga T 1999 Tip-scanning dynamic force microscope using piezoelectric cantilever for full wafer inspection *Japan. J. Appl. Phys.* **38** 7155

[27] Itoh T, Lee C and Suga T 1996 Deflection detection and feedback actuation using a self-excited piezoelectric pb(zr,ti)o[sub 3] microcantilever for dynamic scanning force microscopy *Appl. Phys. Lett.* **69** 2036

[28] Minne S, Adams J, Yaralioglu G, Manalis S, Atalar A and Quate C 1998 Centimeter scale atomic force microscope imaging and lithography *Appl. Phys. Lett.* **73** 1742

[29] Lee C, Itoh T, Ohashi T, Maeda R and Suga T 1997 Development of a piezoelectric self-excitation and self-detection mechanism in PZT microcantilevers for dynamic scanning force microscopy in liquid *J. Vac. Sci. Technol.* B **15** 1559

[30] Lee C, Itoh T, Maeda R and Suga T 1997 Characterization of micromachined piezoelectric PZT force sensors for dynamic scanning force microscopy *Rev. Sci. Instrum.* **68** 2091

[31] Manning L, Rogers B, Jones M, Adams J D, Fuste J L and Minne S C 2003 Self-oscillating tapping mode atomic force microscopy *Rev. Sci. Instrum.* **74** 4220

[32] Adams J, Manning L, Rogers B, Jones M and Minne S 2005 Self-sensing tapping mode atomic force microscopy *Sensors Actuators A* **121** 262

[33] Siechen S, Yang S, Chiba A and Saif T 2009 Mechanical tension contributes to clustering of neurotransmitter vesicles at presynaptic terminals *Proc. Natl Acad. Sci.* **106** 12611

[34] Mutyala M S K, Bandhanadham D, Pan L, Pendyala V R and Ji H 2009 Mechanical and electronic approaches to improve the sensitivity of microcantilever sensors *Acta Mech. Sin.* **25** 1

[35] Smith C S 1954 Piezoresistance effect in germanium and silicon *Phys. Rev.* **94** 42

[36] Richter J, Pedersen J, Brandbyge M, Thomsen E and Hansen O 2008 Piezoresistance in p-type silicon revisited *J. Appl. Phys.* **104** 023715

[37] Park S J, Doll J C and Pruitt B L 2010 Piezoresistive cantilever performance: part I. Analytical model for sensitivity *J. Microelectromech. Syst.* **19** 137

[38] Roark R and Young W 1975 *Formulas for Stress and Strain* (New York: McGraw-Hill)

[39] Gabrielson T, Center U and Warminster P 1993 Mechanical-thermal noise in micromachined acoustic and vibration sensors *IEEE Trans. Electron Devices* **40** 903

[40] Senturia S 2000 *Microsystem Design* (Berlin: Springer)

[41] Masetti G, Severi M and Solmi S 1983 Modeling of carrier mobility against carrier concentration in arsenic-, phosphorus-, and boron-doped silicon *IEEE Trans. Electron Devices* **30** 764

[42] King W P 2005 Design analysis of heated atomic force microscope cantilevers for nanotopography measurements *J. Micromech. Microeng.* **15** 2441

[43] Hooge F 1994 $1/f$ noise sources *Advanced Experimental Methods for Noise Research in Nanoscale Electron Devices* (Dordrecht: Kluwer)

[44] Blom F, Bouwstra S, Elwenspoek M and Fluitman J 1992 Dependence of the quality factor of micromachined silicon beam resonators on pressure and geometry *J. Vac. Sci. Technol. B* **10** 19

[45] Eysden C V and Sader J 2007 Frequency response of cantilever beams immersed in viscous fluids with applications to the atomic force microscope: arbitrary mode order *J. Appl. Phys.* **101** 044908

[46] Spencer R, Fleischer B, Barth P and Angell J 1988 A theoretical study of transducer noise in piezoresistive and capacitive silicon pressure sensors *IEEE Trans. Electron Devices* **35** 1289

[47] Hansen O and Boisen A 1999 Noise in piezoresistive atomic force microscopy *Nanotechnology* **10** 51

[48] Kon S and Horowitz R 2008 A high-resolution MEMS piezoelectric strain sensor for structural vibration detection *IEEE Sensors J.* **8** 2027

[49] Horowitz P and Hill W 1989 *The Art of Electronics* (New York: Cambridge University Press)

[50] DeVoe D and Pisano A 2001 Surface micromachined piezoelectric accelerometers (pixls) *J. Microelectromech. Syst.* **10** 180

[51] Smits J and Choi W 1991 The constituent equations of piezoelectric heterogeneous bimorphs *IEEE Trans. Ultrason. Ferroelectr. Freq. Control* **38** 256
[52] Meng Q, Mehregany M and Deng K 1993 Modeling of the electromechanical performance of piezoelectric laminated microactuators *J. Micromech. Microeng.* **3** 18
[53] Zou Q, Tan W, Kim E S and Loeb G 2008 Single- and triaxis piezoelectric-bimorph accelerometers *J. Microelectromech. Syst.* **17** 45
[54] Trumbore F 1964 Solid solubilities of impurity elements in germanium and silicon *Micro and Thin-film Electronics: Reading* (New York: Holt, Rinehart and Winston) p 177
[55] Isarakorn D, Sambri A, Janphuang P, Briand D, Gariglio S, Triscone J M, Guy F, Reiner J W, Ahn C H and de Rooij N F 2010 Epitaxial piezoelectric MEMS on silicon *J. Micromech. Microeng.* **20** 055008
[56] Hopcroft M A, Nix W D and Kenny T W 2010 What is the Young's modulus of silicon? *J. Microelectromech. Syst.* **19** 229
[57] Tsuchiya T, Hirata M and Chiba N 2005 Young's modulus, fracture strain, and tensile strength of sputtered titanium thin films *Thin Solid Films* **484** 245
[58] Wright A F 1997 Elastic properties of zinc-blende and wurtzite AlN, GaN, and InN *J. Appl. Phys.* **82** 2833
[59] Dubois M and Muralt P 1999 Properties of aluminum nitride thin films for piezoelectric transducers and microwave filter applications *Appl. Phys. Lett.* **74** 3032
[60] Tsubouchi K and Mikoshiba N 1985 Zero-temperature-coefficient SAW devices on AlN epitaxial films *IEEE Trans. Sonics Ultrason.* **32** 634
[61] Doll J C, Petzold B C, Ninan B, Mullapudi R and Pruitt B L 2010 Aluminum nitride on titanium for CMOS compatible piezoelectric transducers *J. Micromech. Microeng.* **20** 025008
[62] Sinha N, Wabiszewski G E, Mahameed R, Felmetsger V V, Tanner S M, Carpick R W and Piazza G 2009 Piezoelectric aluminum nitride nanoelectromechanical actuators *Appl. Phys. Lett.* **95** 053106
[63] Tonisch K, Cimalla V, Foerster C, Romanus H, Ambacher O and Dontsov D 2006 Piezoelectric properties of polycrystalline AlN thin films for MEMS application *Sensors Actuators A* **132** 658
[64] Martin F, Muralt P, Dubois M and Pezous A 2004 Thickness dependence of the properties of highly c-axis textured AlN thin films *J. Vac. Sci. Technol.* A **22** 361
[65] Watanabe S, Fujiu T and Fujii T 1995 Effect of poling on piezoelectric properties of lead zirconate titanate thin films formed by sputtering *Appl. Phys. Lett.* **66** 1481
[66] Kanno I, Fujii S, Kamada T and Takayama R 1997 Piezoelectric properties of c-axis oriented $Pb(Zr,Ti)O_3$ thin films *Appl. Phys. Lett.* **70** 1378
[67] Muralt P, Kohli M, Maeder T, Kholkin A, Brooks K, Setter N and Luthier R 1995 Fabrication and characterization of PZT thin-film vibrators for micromotors *Sensors Actuators A* **48** 157
[68] Shepard J, Chu F, Kanno I and Trolier-McKinstry S 1999 Characterization and aging response of the d_{31} piezoelectric coefficient of lead zirconate titanate thin films *J. Appl. Phys.* **85** 6711
[69] Dubois M A and Muralt P 1999 Measurement of the effective transverse piezoelectric coefficient $e_{31,f}$ of AlN and $Pb(Zr_x,Ti_{1-x})O_3$ thin films *Sensors Actuators* A **77** 106
[70] Chen H D, Udayakumar K R, Cross L E, Bernstein J J and Niles L C 1995 Dielectric, ferroelectric, and piezoelectric properties of lead zirconate titanate thick films on silicon substrates *J. Appl. Phys.* **77** 3349
[71] Udayakumar K R, Schuele P J, Chen J, Krupanidhi S B and Cross L E 1995 Thickness-dependent electrical characteristics of lead zirconate titanate thin films *J. Appl. Phys.* **77** 3981
[72] Chu J, Itoh T, Lee C, Suga T and Watanabe K 1997 Novel high vacuum scanning force microscope using a piezoelectric cantilever and the phase detection method *J. Vac. Sci. Technol.* B **15** 1551
[73] Neuman K C and Nagy A 2008 Single-molecule force spectroscopy: optical tweezers, magnetic tweezers and atomic force microscopy *Nature Methods* **5** 491
[74] Li M, Tang H X and Roukes M L 2007 Ultra-sensitive NEMS-based cantilevers for sensing, scanned probe and very high-frequency applications *Nature Nanotechnol.* **2** 114